



PCCP

Tuning the UV spectrum of PAHs by means of different N-doping types taking pyrene as paradigmatic example: categorization via valence bond theory and high-level computational approaches

Journal:	<i>Physical Chemistry Chemical Physics</i>
Manuscript ID	CP-ART-05-2020-002688.R2
Article Type:	Paper
Date Submitted by the Author:	10-Sep-2020
Complete List of Authors:	Xin, Shao; Tianjin University Aquino, Adelia; University of Vienna, Otyepka, Michal; Palacky University Olomouc, Physical Chemistry Nachtigallova, Dana; Institute of Organic Chemistry and Biochemistry, Molecular Modeling Lischka, Hans; University of Vienna, Institute for Theoretical Chemistry and Structural Biology

SCHOLARONE™
Manuscripts

Tuning the UV spectrum of PAHs by means of different N-doping types taking pyrene as paradigmatic example: categorization via valence bond theory and high-level computational approaches

Shao Xin,^a Adelia J.A. Aquino,^{a,b} Michal Otyepka,^c Dana Nachtigallová,^{c,d*} Hans Lischka^{a,e*}

^aSchool of Pharmaceutical Science and Technology, Tianjin University, Tianjin 300072, PR China

^bDepartment of Mechanical Engineering, Texas Tech University, Lubbock, TX, 79409, USA

^cRegional Centre of Advanced Technologies and Materials, Palacký University, 78371 Olomouc, Czech Republic

^dInstitute of Organic Chemistry and Biochemistry v.v.i., The Czech Academy of Sciences, Flemingovo nám. 2, 16610 Prague 6, Czech Republic

^eDepartment of Chemistry and Biochemistry, Texas Tech University Lubbock, TX 79409-1061, USA

Abstract

Tuning of the electronic spectra of carbon dots by means of inserting heteroatoms into the π -conjugated polycyclic aromatic hydrocarbon (PAH) system is a popular tool to achieve a broad range of absorption and emission frequencies. Especially nitrogen atoms have been used successfully for that purpose. Despite the significant progress achieved with these procedures, the prediction of specific shifts in the UV-vis spectra and the understanding of the electronic transitions is still a challenging task. In this work, high-level quantum chemical methods based on multireference (MR) and single-reference (SR) methods have been used to predict the effect of different nitrogen doping patterns inserted into the prototypical PAH pyrene on its absorption spectrum. Furthermore, a simple classification scheme based on valence bond (VB) theory and the Clar sextet rule in combination with the harmonic oscillator measure of aromaticity (HOMA) index was applied to arrange the different doping structures into groups and rationalize their electronic properties. The results show a wide variety of mostly redshifts in the spectra as compared to the pristine pyrene case. The most interesting doping structures with the largest red shifts leading to absorption energies below one eV could be readily explained by the occurrence of diradical VB structures in combination with Clar sextets. Moreover, analysis of the electronic transitions computed with MR methods showed that several of low-lying excited states possess double-excitation character, which cannot be realized by the popular SR methods and, thus, are simply absent in the calculated spectra.

1 Introduction

Due to their outstanding optical properties, carbon dots (CD) constitute a fascinating new carbon-based material with interesting applications in materials science, chemistry, biosensing and several other fields.¹⁻⁵ Their chemical modification, which includes also chemical doping, provides a promising strategy to modulate their electronic properties which should convert them to materials with even better performance than their pristine counter-partners.⁶ In particular, nitrogen doping changes the electronic properties of CDs, which can be efficiently used to design systems such as sensors,⁷ electro-catalysts in redox reactions,⁸⁻¹² systems with capabilities of electrochemical energy storage,¹³ photocatalysts,¹⁴⁻¹⁷ and battery constructions.¹⁸ Their optical properties with the photoluminescence quantum yield up to 75% make them efficient fluorescence probes¹⁹⁻²³ and light-emitting diodes²⁴. In this context, the red-shift of the fluorescence is of great relevance e.g. for bioimaging applications because near infra-red light exhibits deeper tissue penetration.²⁵

Despite the large potential of just-mentioned N-doped CDs, understanding of the optical spectra and finding materials which possess appropriately red-shifted UV and fluorescence properties represent still a challenging task for experimental as well as computational research. Photoemission spectra of N-doped CD's reported in several experimental studies²⁶⁻³³ demonstrate a complex picture, complicated, among others, by different doping forms, such as graphitic-, graphitic-edge- pyridinic- and amino-forms of N-dopants. Inconsistent observations originate from a high heterogeneity in CD sizes and shapes,³⁴ different surface functional groups and defects. The complexity of spectra in the UV and visible regions is demonstrated by significant variations in emission colors and fluorescence quantum yield, in the range of 6-80%,³⁵ of CDs prepared under different conditions and using different amino-precursors.^{36, 37} In view of the just-described complexity of the CDs, interesting experimental attempts have been made to explain the optical properties of the CDs based on mixtures of model PAHs including relatively small PAHs such as pyrene.³⁸

The situation is becoming even more complex in case of N doping. The effects of nitrogen atoms depend also strongly on the location within CD structures.³⁹⁻⁴¹ When an N atom replaces a

CH group, leading to a pyridinic form, the N-lone pair is located in the molecular plane and only one electron is contributed to the π -system, as occurs in non-doped systems by carbon atoms also. In contrast, in graphitic and graphitic-edge structures, only the C-atom is replaced and the N-atom thus contributes two electrons to the π -system. The different types of doping and corresponding variations in the electronic structure are the reasons for the complex character of optical spectra as demonstrated in many experimental and computational studies.^{26, 35, 36, 42-47} Based on density functional theory (DFT) calculations and time-dependent DFT (TD-DFT) spectra calculations significant red-shifts in UV absorption spectra were found by graphitic nitrogens, while other nitrogen substitutions had smaller effects.^{43, 45, 48, 49}

Previous investigations on the electronic ground states of N-doped PAHs⁵⁰⁻⁵³ based on highly correlated multireference methods showed, that by this process the biradicaloid character could be enhanced significantly. Biradicaloid character has to be expected for the doped pyrenes as well, and will not only affect the ground state but also excited states. In spite of the extensive work spent on detailed spectroscopic investigations of CDs, spectroscopic data on specific N-doped PAHs occurring in CDs are extremely rare and to the best of our knowledge, there are no experimental data for the studied systems available. However, theoretical calculations are well suited to shed light into the spectroscopic characteristics of different doping patterns and to aid in the development of efficient new materials. Therefore, following the above-mentioned experimental approaches of modeling the spectroscopic properties of CDs by means of selected PAHs, we have chosen pyrene as a paradigmatic reference PAH, which is well suited to study N-doping effects on UV spectra in detail. For that purpose, doping with two N atoms in various positions have been investigated, resulting in pyridinic-, graphitic-edge and graphitic doped structures. Multireference calculations of the type density functional theory/multireference configuration interaction (DFT/MRCI)⁵⁴⁻⁵⁷ and strongly contracted-n-electron valence state perturbation theory to second order (SC-NEVPT2)^{58, 59} have been performed in comparison with popular single reference methods such as second-order algebraic diagrammatic construction (ADC(2)) calculations^{60, 61} and time-dependent density functional theory (TD-DFT), employing B3LYP⁶² and CAM-B3LYP⁶³ functionals. Their reliability for the description of the excited states of non-doped CD models was demonstrated in calculations of polyacenes⁶⁴ and PAHs based on pyrene and coronene.⁶⁵⁻⁶⁷ In these investigations the DFT/MRCI method showed remarkably good agreement with available

experimental data and is, thus, used for characterization of the excited states of N-doped pyrene and evaluation of other, less computationally demanding methods.

It has been shown in previous examples for N-doping (see e.g. Refs. 53 and 68), that very simple tools of valence bond (VB) theory combined with Clar's sextet rule⁶⁹ can be very useful in disentangling the maze of different doping options. It is one major issue of this work to show that this is also true for the quite large manifold of 34 different doping cases, where these straightforward prescriptions can be very useful for categorizing and possibly selecting different doping options.

2 Computational methods

Ground-state geometries of all structures were optimized at the DFT level using the B3-LYP⁶² functional together with the D3 empirical dispersion correction by Grimme et al.⁷⁰ and the long-range corrected functional CAM-B3LYP.⁶³ Furthermore, second-order Møller-Plesset perturbation theory (MP2)⁷¹ was used in combination with the scaled opposite-spin (SOS) correction.⁷² Reference calculations on ground-state stabilities have been performed using the domain-based local pair natural orbital (DLPNO)⁷³-coupled cluster with singles, doubles and noniterative triples (CCSD(T))^{74, 75} approach using the SOS-MP2 geometry. All calculations were performed with the triple-zeta valence polarization def2-TZVP⁷⁶ basis set. In case of the DFT methods, the vertical excitations were calculated by means of TD-DFT at the optimized geometry of the respective method. *Ab initio* ADC(2) calculations^{60, 61} employing the resolution-of-the-identity (RI) approximation⁷⁷ were performed based on SOS-MP2 geometries. Multireference (MR) calculations for excited states were carried at the DFT/MRCI level developed by Grimme and Waletzke⁵⁴ and redesigned by Marian et al.⁵⁵⁻⁵⁷ and by means of the SC-NEVPT2^{58, 59} method. As reference space, a complete active space (CAS) for eight electrons and eight orbitals, CAS(8,8), was used in all MR calculations. For SC-NEVPT2, the orbitals were determined from a CASSCF(8,8) calculation averaged over 10 states. In case of DFT/MRCI, an initial reference wavefunction was chosen as a CAS(8,8) restricted by double-excitations; an energy cutoff of 0.8 Hartree was used together with the parameter set "short" as explained in Refs. ^{56, 57} This reference was iteratively improved by including all configurations exceeding a weight of 0.003 for the next iteration as recommended in Ref. 56. Convergence was achieved by the requirement that energy

difference between different iteration were below 10^{-5} Hartree for all roots. A maximum of four iterations was performed. The orbitals were calculated in the latter case from Becke's hybrid exchange-correlation functional (BHLYP).⁷⁸ For the MR calculations the geometries obtained with the B3LYP approach were employed.

Harmonic frequency calculations were performed in all cases to verify by the absence of imaginary frequencies that the structures were minima. In case of the pyridinic doping, all structures were planar. For the graphitic and graphitic-edge doping cases, some planar structures had imaginary frequencies related to out-of-plane motions. The occurrence of imaginary frequencies was not unanimous for all methods. Re-optimization of these structures by removing planarity constraints led to minima in all cases. The deviations from planarity were in most cases quite small, though. The energetic stabilization was largest for pyr-graphitic-2 and -3 with about 4 kcal/mol. In all other cases the energetic effects were significantly smaller. There were, however, two cases, pyr-graphitic-edge-3 and -7 (see below), where the two N atoms were direct neighbors and the out-of-plane displacement of the connected H atoms could not be ignored. Thus, these two isomers were considered in their nonplanar structures. Calculated excitation energies performed for the most critical cases showed changes less than 0.1 eV. Because of the small energetic effects and the advantage of having the same type of structures for all methods, we decided to stay with the planar structures, except for the two exceptions mentioned just above.

The harmonic oscillator measure of aromaticity (HOMA)^{79, 80} has been used as measure for the aromaticity of the benzene rings in the doped pyrene isomers. Using Kekulé benzene as reference, the HOMA index of a ring

$$\text{HOMA} = 1 - \frac{\alpha}{N} \sum_i (R_{\text{opt}} - R_i)^2 \quad (1)$$

indicates how much the bond distances R_i of a molecule differ from optimal values R_{opt} . The normalization constant α keeps the HOMA index as zero for Kekulé benzene. N counts the number of atoms in the ring. The R_{opt} values for CC bonds are 1.388 Å, for CN bonds 1.334 Å and for NN bonds 1.309 Å. Corresponding α values are 257.7, 93.52 and 130.33.

Effectively unpaired densities $d_{\text{U(H-L)}}(\mathbf{r})$ ^{81, 82} were calculated by means of the nonlinear formula developed by Head-Gordon

$$d_{U(H-L)}(\mathbf{r}) = \sum_{i=HONO}^{LUNO} n_i^2 (2 - n_i)^2 \phi_{NO,i}^2(\mathbf{r}) \quad (2)$$

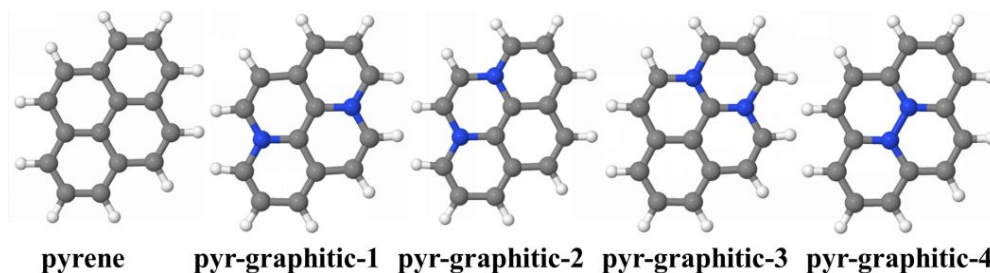
in order to assess the radical nature of selected structures; n_i is the occupation of the natural orbital (NO) $\phi_{NO,i}$. The summation is restricted in the present case to the highest occupied (HONO) and lowest unoccupied (LUNO) NOs.⁵¹

All DFT/B3LYP, TD-B3LYP, SOS-RI-MP2, ADC(2) calculations were carried out using the TURBOMOLE 7.2 program.⁸³ Both DFT/CAM-B3LYP and TD-CAM-B3LYP computations were performed with the Gaussian 09 program.⁸⁴ The ORCA 4.0 program system⁸⁵ was used for the SC-NEVPT2 and DLPNO-CCSD(T) calculations.

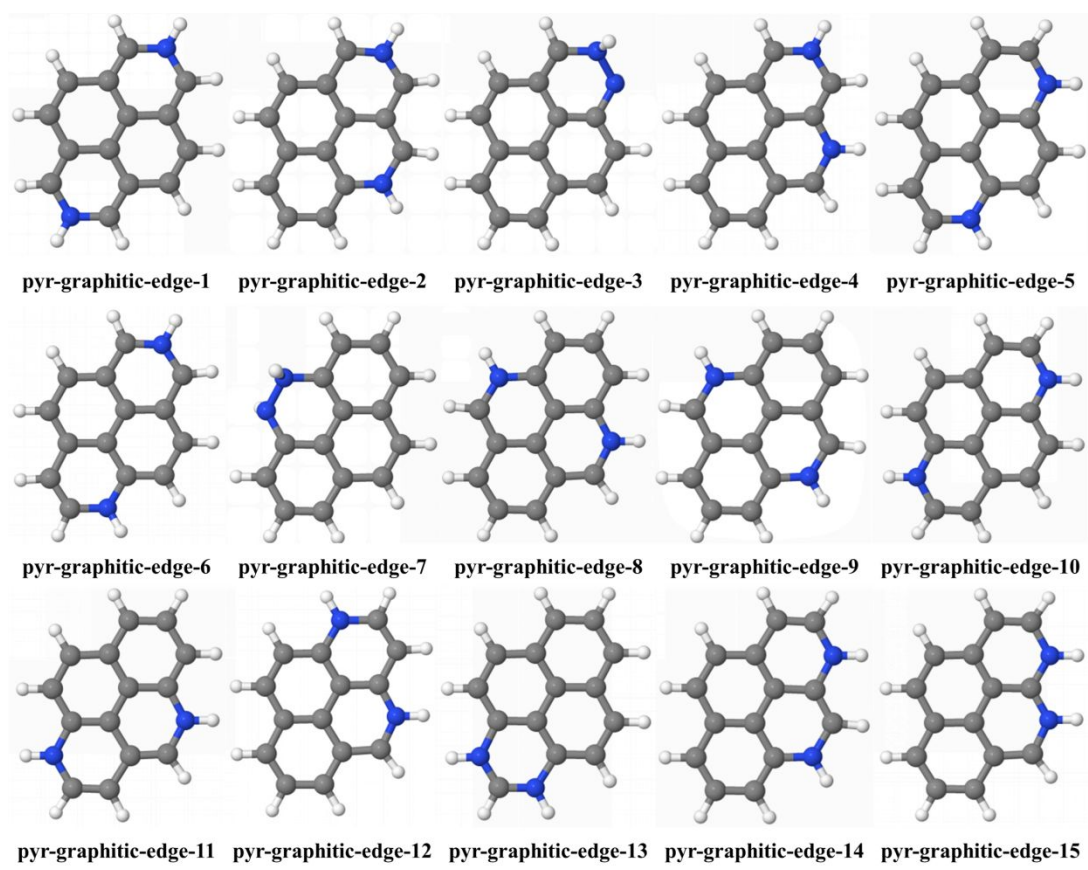
3 RESULTS

3.1 Ground state

All the N-doped pyrenes considered in the study were constructed by positioning two N atoms symmetrically in pyrene. These structures are displayed in Scheme 1 for graphitic doping, in Scheme 2 for graphitic-edge doping and in Scheme 3 for pyridinic doping. Scheme 1 shows also the pristine pyrene. The Cartesian coordinates of the structures optimized in the ground state and total energies are collected in the Electronic Supplementary Information (ESI) for the B3LYP, CAM-B3LYP and SOS-MP2 methods.



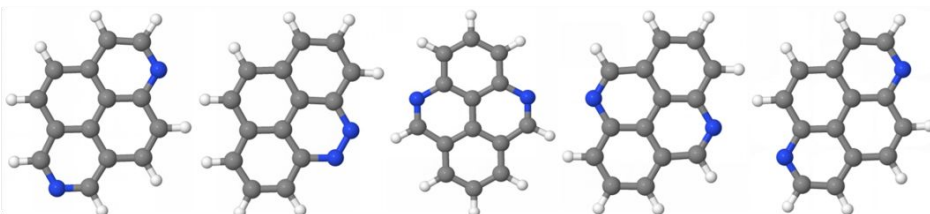
Scheme 1 Pristine pyrene and graphitic N-doping of pyrene. The total number of π electrons is 16 for pyrene and 18 for the pyr-graphitic structures.



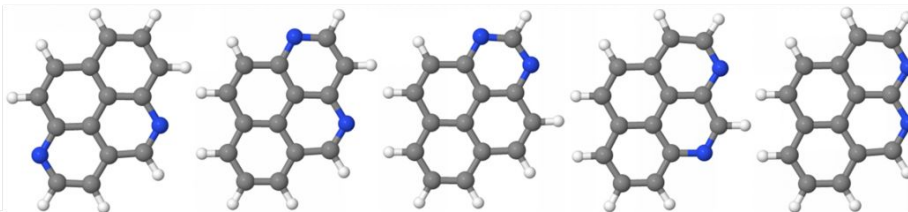
Scheme 2 Graphitic-edge N-doping of pyrene. The total number of π electrons is 18 for the pyr-graphitic-edge structures.



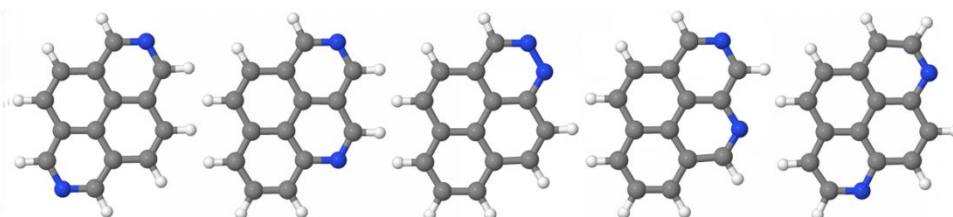
pyr-pyridinic-1 pyr-pyridinic-2 pyr-pyridinic-3 pyr-pyridinic-4 pyr-pyridinic-5



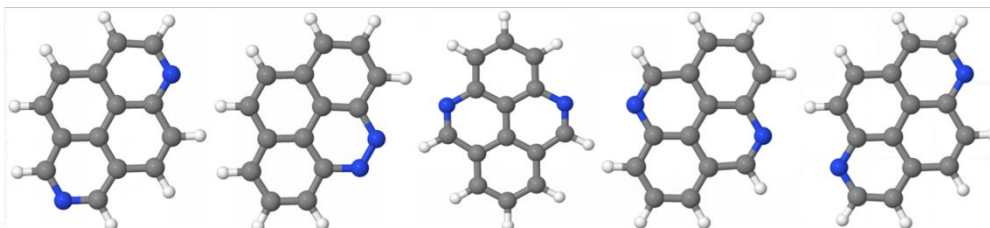
pyr-pyridinic-6 pyr-pyridinic-7 pyr-pyridinic-8 pyr-pyridinic-9 pyr-pyridinic-10



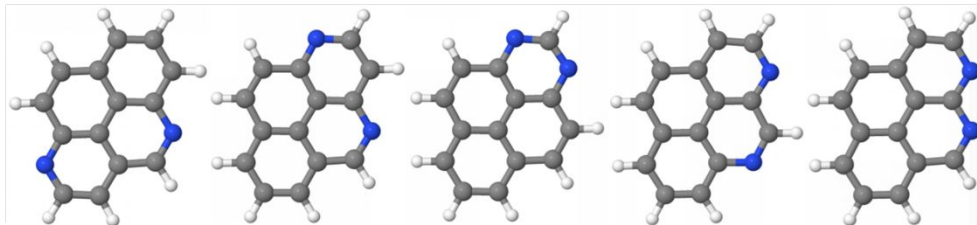
pyr-pyridinic-11 pyr-pyridinic-12 pyr-pyridinic-13 pyr-pyridinic-14 pyr-pyridinic-15



pyr-pyridinic-1 pyr-pyridinic-2 pyr-pyridinic-3 pyr-pyridinic-4 pyr-pyridinic-5



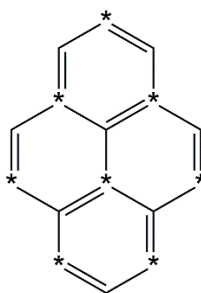
pyr-pyridinic-6 pyr-pyridinic-7 pyr-pyridinic-8 pyr-pyridinic-9 pyr-pyridinic-10



pyr-pyridinic-11 pyr-pyridinic-12 pyr-pyridinic-13 pyr-pyridinic-14 pyr-pyridinic-15

Scheme 3 Pyridinic N-doping of pyrene. The total number of π electrons is 16 for the pyridinic N-doped structures.

The trends of the relative stabilities of different doping structures can be rationalized in terms of their resonance structures, in particular the possibility of showing a Kekulé structure (labelled as KEK) electronic configuration or a diradical structure (labelled as DR), the number of Clar sextets,⁶⁹ as well as the number of carbon atoms separating nitrogen atoms (denoted as NS). Since pyrene is an alternant hydrocarbon,⁸⁶ NS odd denotes two N atoms located in the same sublattice (either starred or unstarred, Scheme 4), whereas for NS even the two N atoms belong to different sublattices. The combination of a Clar sextet together with either a Kekulé structure is denoted as Clar(KEK). The case where a Clar sextet occurs only together with a diradical structure is called Clar(DR).



Scheme 4 Pyrene structure as an alternant hydrocarbon as indicated by the sequence of starred and unstarred C atoms.

3.1.1 Graphitic structures

The ground state stabilities of pyr-graphitic structures with respect to the most stable pyr-graphitic structure (pyr-graphitic-1) are compared in Figure 1 and Table 1 for SOS-MP2, B3LYP, CAM-B3LYP, DFT/MRCI and DLPNO-CCSD(T) levels. All methods show quite similar trends. DL-PNO-CCSD(T) and SOS-MP2 always agree very well, some discrepancies with the other methods can be seen for the pyr-graphitic-2 case where especially CAM-B3LYP more significantly overestimates the instability with respect pyr-graphitic-1. The pyr-graphitic-edge-8 structure also shows some differences

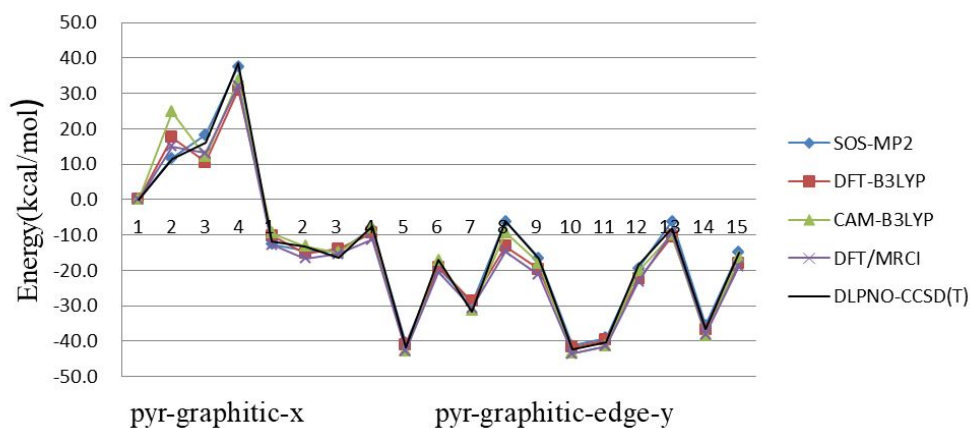
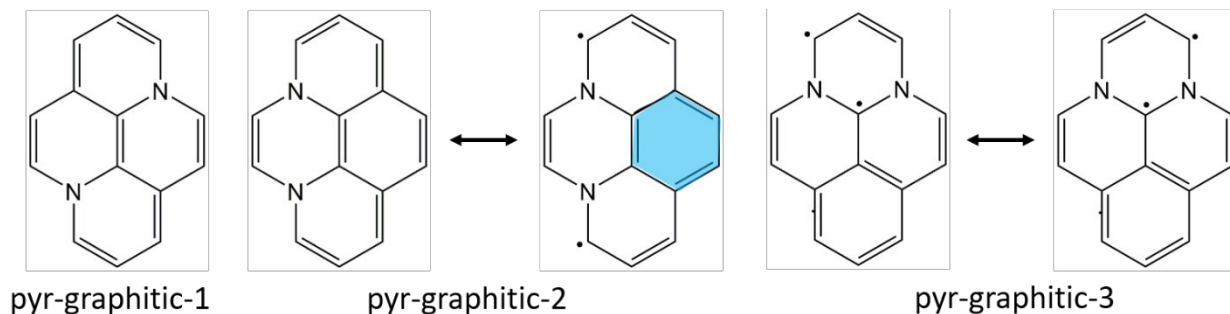


Figure 1 Ground state relative energies (in kcal/mol) of pyr-graphitic and pyr-graphitic-edge structures with respect to pyr-graphitic-1 calculated at the SOS-MP2, B3LYP, CAM-B3LYP, DFT/MRCI and DLPNO-CCSD(T) levels. The def2-TZVP basis set was used always.

In the case of the most stable pyr-graphitic-1 and pyr-graphitic-2 structures (Table 1), the nitrogen atoms are separated by two carbons ($NS=2$). In both cases, a Kekulé (KEK) structure without Clar sextets exists (Scheme 5). The latter, however, possesses also a diradical VB structure with one Clar sextet (Clar(DR)) and, thus, should possess higher reactivity. According to the calculated HOMA values (Figure 2 and Figure S1 of the Supporting Information (SI) for a complete collection) there is a significant contribution of the Clar sextet in this case. This conclusion is also confirmed by the 11.8 kcal/mol higher energy than pyr-graphitic-1 (Figure 1 and Table 1). The same diradical VB structure with the Clar sextet can be obtained also for pyr-graphitic-3 with $NS=1$, which is less stable than pyr-graphitic-1, with no possibility to form a KEK electronic structure. Note that the ordering of pyr-graphitic-2 and pyr-graphitic-3 reverses at the DFT levels. DFT/MRCI gives approximately the same stability of the two isomers. The increasing diradicaloid character deduced qualitatively, is also confirmed by the CAS self-consistent field calculations preceding the SC-NEVPT2 calculations, in which the HONO/LUNO pairs assume the values 1.89/0.04e, 1.23/0.89e and 1.03/1.00e for pyr-graphitic-1 to -3, respectively. The H-L unpaired densities (Eq. (2)) shown for pyr-graphitic-2 and -3 (Figure 3) agree nicely with the

respective VB structures (Scheme 5). The lowest stability of pyr-graphitic-4 with NS=0 results probably from the close proximity of the two N atoms.



Scheme 5. Selected VB structures for pyr-pyridinic structures. Clar sextets are shown in color.

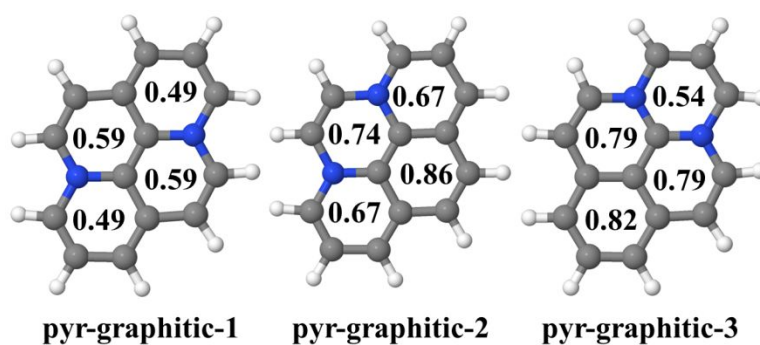


Figure 2. HOMA values computed for three graphitic structures using B3LYP calculations.

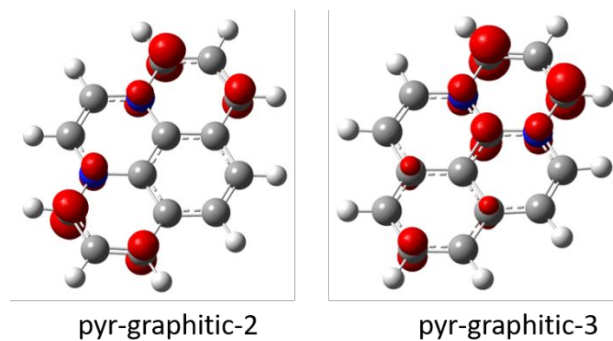


Figure 3. Plot of the unpaired densities (Eq. (2)) using the HONO and LUNO orbitals for the ground state calculated from SA-CASSCF calculations.

Table 1 Relative energies (in kcal/mol) and ground-state character of graphitic N-doped pyrenes (pyr-graphitic-x) calculated at the B3LYP, SOS-MP2 and CAM-B3LYP levels^a

	pyr-graphitic-x			
	x=1	x=2	x=3	x=4
	KEK(2)	KEK(2)/ Clar(DR)	Clar(DR)(1)	KEK(0)
DFT- B3LYP	0.0	17.6	10.5	31.0
SOS-MP2	0.0	11.8	18.3	37.7
CAM- B3LYP	0.0	24.7	12.1	33.7
DFT/MRCI	0.0	15.1	13.1	32.1
DLPNO- CCSD(T)	0.0	11.4	16.0	38.6

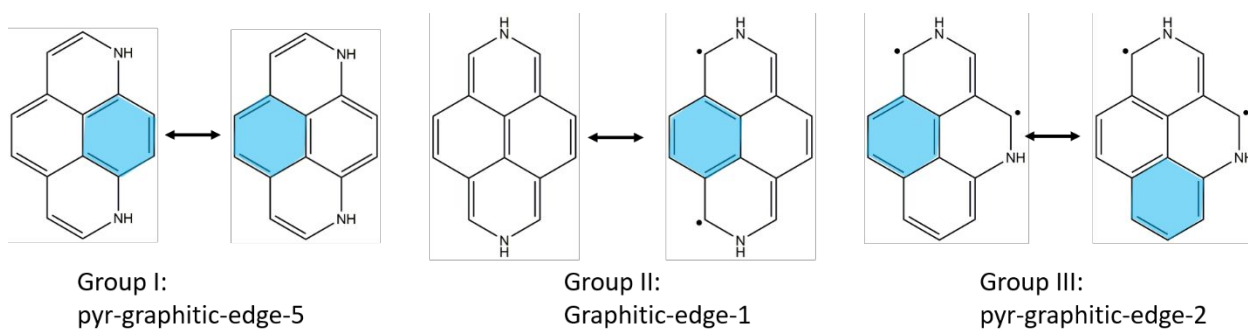
^a numbers in parentheses denote NS values.

3.1.2 Graphitic-edge doping

Doping in graphitic-edge positions results in more stable structures compared to graphitic doping (Figure 1 and Table 2). As for the graphitic doping cases, possibilities to form the KEK VB structure, which exist only for even NS numbers, and structures with Clar sextets are the key factors which determine their relative stabilities. In the following discussions, the different isomers are arranged into three groups based on the character of the ground state wavefunctions (Table 2 and Scheme 6): (I) structures pyr-graphitic-edge-3, -5, -7, -10, -11 and -14 (classified as KEK, Clar(KEK)), (II) structures pyr-graphitic-edge-1, -4 and -9 (classified as KEK, Clar(DR)) and (III) structures pyr-graphitic-edge-2, -6, -8, -12, -13 and -15 (classified as Clar(DR)).

The most stable systems, pyr-graphitic-edge-10 (most stable) and pyr-graphitic-edge-5, -7, -10, -11 and -14, all belong to group I (Table 2). The reason for this stability is that they can adopt Clar(KEK) VB structures (see Scheme 6 for an example). The ordering among them is further determined by NS; structures with larger NS are more stable. The HOMA values provide additional information on the resonance character of VB structures. For example, the large values

of two fused benzene rings in pyr-graphitic-edge-5 (Figure 4) indicate the existence of two resonant structures with one Clar sextet each (Scheme 6). Note that a relatively large stability is observed also in the case of pyr-graphitic-edge-7, although with $NS=0$ and the hydrogen atoms moved out from the molecular plane. Pyr-graphitic-edge-3, also with $NS=0$, is the least stable of this group. The favorable stability of pyr-graphitic-edge-7 vs. the edge-3 isomer can be rationalized by their HOMA values. Following the condition that Clar sextets cannot exist on adjacent rings, two resonant structures with only one Clar sextet each (Scheme 7), with HOMA values of 0.87 and 0.81 (Figure 4), contribute to the resulting electronic structure of pyr-graphitic-3. On the other hand, two non-fused Clar sextets with significantly large aromaticity (HOMA values of 0.92) coexist in pyr-graphitic-7. The remaining structures with even NS number (group II) and structures with odd NS numbers (group III), are less stable (see Table 2). The graphitic-edge-1 example of the group II structure given in Scheme 6 shows the resonance of a quinoid structure without Clar sextet and a biradical structure with one Clar sextet. The small HOMA value (0.13, Figure 4) of the corresponding ring shows an almost anti-aromatic character and preference of the quinoid structure. The HOMA values of pyr-graphitic-edge-2, group III (Figure 4), indicate the existence of two resonant structures with biradical character and one Clar sextet each as shown in Scheme 6.



Scheme 6. Selected VB structures for pyr-graphitic-edge structures. Clar sextets are shown in color.

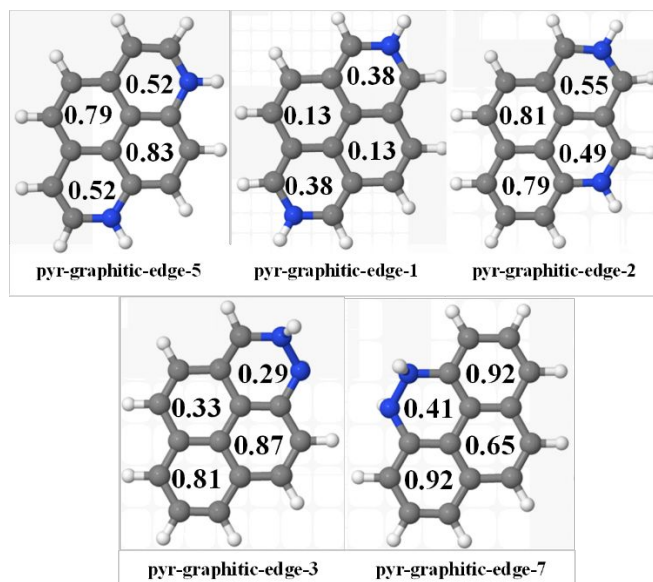
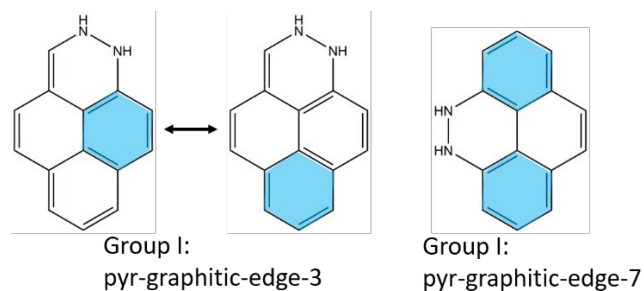


Figure 4. HOMA values computed for selected graphitic-edge structures using B3LYP calculations.



Scheme 7. VB structures for pyr-graphitic-edge structures. Clar sextets are shown in color.

Table 2 Relative energies (in kcal/mol) of graphitic-edge N-doped pyrene (pyr-graphitic-edge-y) with respect to pyr-graphitic-1 calculated at the B3LYP, SOS-MP2 and CAM-B3LYP levels.^a

	pyr-graphitic-edge-y				
	y=1 KEK(6)/ Clar(DR)	y=2 DR(3)	y=3 KEK(0)/ Clar(KEK)	y=4 KEK(2)/ Clar(DR)	y=5 KEK(4)/ Clar(KEK)
B3LYP	-10.2	-15.2	-13.9	-9.4	-41.1
SOS-MP2	-12.6	-14.4	-14.7	-8.1	-40.6
CAM-B3LYP	-9.5	-13.3	-15.0	-8.1	-42.7
DFT/MRCI	-12.8	-16.6	-15.3	-11.3	-42.7

DLPNO-CCSD(T)	-11.9	-13.2	-16.6	-7.5	-41.9
	y=6	y=7	y=8	y=9	y=10
	DR(5)	KEK(0)/ Clar(KEK)	DR(3)	KEK(4) Clar(DR)	KEK(4)/ Clar(KEK)
B3LYP	-19.2	-28.7	-13.2	-19.6	-41.7
SOS-MP2	-19.2	-29.4	-6.1	-16.5	-41.3
CAM-B3LYP	-17.1	-31.3	-9.3	-17.9	-43.4
DFT-MRCI?	-20.5	-30.6	-14.7	-21.3	-43.5
DLPNO-CCSD(T)	-17.1	-31.7	-6.1	-16.7	-42.5
	y=11	y=12	y=13	y=14	y=15
	KEK(4)/ Clar(KEK)	DR(3)	DR(1)	KEK(2)/ Clar(KEK)	DR(1)
B3LYP	-39.7	-22.4	-10.5	-36.6	-18.1
SOS-MP2	-39.1	-19.5	-6.2	-35.4	-14.8
CAM-B3LYP	-41.3	-20.1	-9.9	-38.3	-16.4
DFT-MRCI?	-41.4	-23.1	-9.3	-38.0	-18.8
DLPNO-CCSD(T)	-40.4	-18.6	-8.2	-36.7	-15.1

^aNS values are given in parentheses.

3.1.3 Pyridinic doping

The electronic properties of pyridinic doping cases closely resemble those of pyrene, i.e. they possess KEK structures regardless of N-doping positions. Contrary to the previous cases, the distribution of relative energies (Figure 5, Table 3) are relatively uniform, with a slight preference of structures with nitrogens located close to the zig-zag-type edge, as documented with the most stable pyr-pyridinic-13 (Scheme 3). The only exceptions are pyr-pyridinic-3 and -7 with NS=0 which are by 25.2 and 27.4 kcal/mol (DLPNO-CCSD(T)), respectively, less stable. Note, that the DFT/MRCI approach overestimates the instability of pyr-pyridinic-3 with respect to the most stable pyr-pyridinic-13.

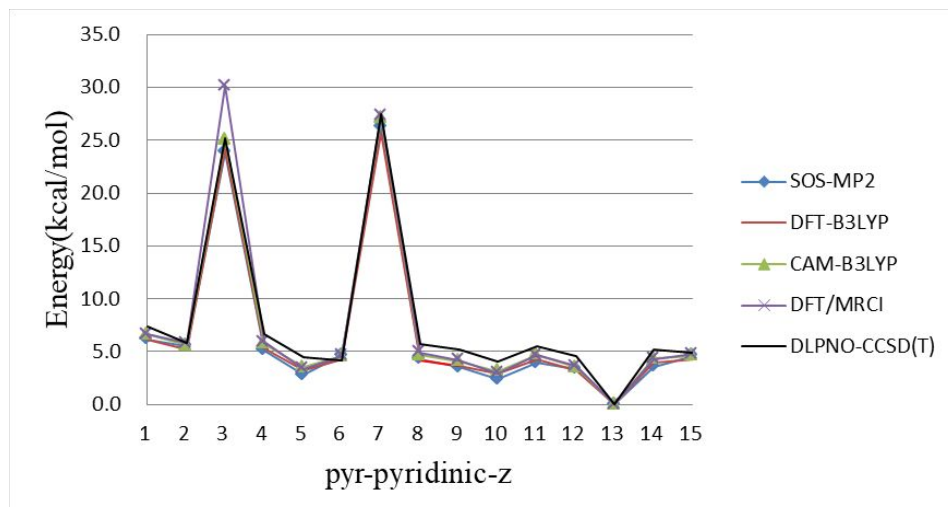


Figure 5 Ground state relative energies (in kcal/mol) with respect to pyr-pyridinic-13 calculated at the SOS-MP2, B3LYP, CAM-B3LYP, DFT/MRCI and DLPNO-CCSD(T) levels. The def2-TZVP basis set was used always.

Table 3 Relative energies (in kcal/mol) for pyridinic N-doped pyrenes (pyr-pyridinic-z) at the B3LYP, SOS-MP2 and CAM-B3LYP levels.^a

	pyr-pyridinic-z				
	z=1	z=2	z=3	z=4	z=5
	KEK(6)	KEK(3)	KEK(0)	KEK(2)	KEK(4)
B3LYP	6.1	5.2	24.1	5.3	3.3
SOS-MP2	6.2	5.5	23.9	5.1	2.8
CAM-B3LYP	6.6	5.6	25.1	5.8	3.5
DFT/MRCI	6.6	5.8	30.1	5.9	3.4
CCSD(T)	7.4	5.8	25.2	6.6	4.5
	z=6	z=7	z=8	z=9	z=10
	KEK(5)	KEK(0)	KEK(3)	KEK(4)	KEK(4)
B3LYP	4.2	25.7	4.2	3.7	2.9
SOS-MP2	4.6	26.2	4.3	3.5	2.4
CAM-B3LYP	4.6	27.1	4.7	4.1	3.2
DFT/MRCI	4.6	27.3	4.9	4.2	2.9
CCSD(T)	4.2	27.4	5.7	5.2	4.1
	z=11	z=12	z=13	z=14	z=15
	KEK(4)	KEK(3)	KEK(1)	KEK(2)	KEK(1)
B3LYP	4.2	3.2	0.0	4.0	4.3
SOS-MP2	3.9	3.3	0.0	3.6	4.6

CAM-B3LYP	4.7	3.5	0.0	4.3	4.6
DFT-MRCI?	4.7	3.6	0.0	4.3	4.8
DLPNO-CCSD(T)	5.5	4.6	0.0	5.2	4.9

^aNS values are given in parentheses

3.2 Excited states

The changes of the character of the electronic ground state caused by the nitrogen doping result in an increased complexity of the electronic excitation spectra with respect to pyrene. In the following discussion we want to analyze the effect of doping at different sites on the electronic spectrum and show the multitude of situations that can occur. The discussion will be governed by the presentation of achievable redshifts of the lowest excited states, especially of S_1 , and further by the characterization of excited states, i.e. singly and doubly excited $\pi \rightarrow \pi^*$ states ($n \rightarrow \pi^*$ states also for the pyridinic structures). The occurrence of doubly excited states is of great interest since they are not accessible by standard single reference methods, but could play an important role for the internal conversion process to S_1 after photoexcitation. In the absence of systematic experimental data, the DFT/MRCI results will be considered as most reliable reference.

3.2.1 Graphitic structures

Figure 6 shows the evolution of the S_1 state of the graphitic doping structures for the different methods. The experimental S_1 excitation energy for pyrene itself amounts to 3.41 eV (L_b state).⁸⁷ The computed value of 3.56 eV (DFT/MRCI, Table S1) is in good agreement with it and also with the recent result of a calculation based on generalized multi-configuration quasi-degenerate perturbation theory.⁸⁸ The complete list of excitation energies computed for the first ten states, oscillator strengths and the classification in terms of single (S) and double (D) excitations can be found in Table S1 of the ESI. All methods agree on the strong red shifts in the range of 2.2 to 3.2 eV. There are some discrepancies though in terms of methods. Most notable is the too large value for the excitation energy obtained by TD-CAM-B3LYP for pyr-graphitic-4. The large shift regarding pyrene leads to remarkable low excitation energies of 0.61 eV and 0.43

eV (DFT/MRCI) for pyr-graphitic-2 and -3, respectively. This agrees well with the partial diradicaloid character of the ground state as indicated in Scheme 5. Pyr-graphitic-4 is a similar case, but probably of less relevance because its significantly decreased stability as compared to the other graphitic structures.

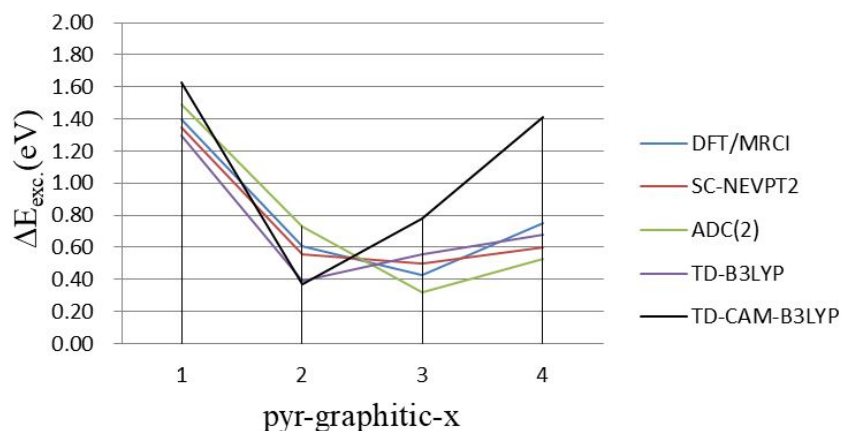


Figure 6 Vertical excitation energies to the S_1 state for graphitic doping structures for all methods using the def2-TZVP basis (pyrene exp. (L_b) 3.41 eV⁸⁷).

The optical spectra are illustrated in more detail for pyr-graphitic-1 and -3 (Figure 7). The spectra of the remaining two graphitic doping cases are displayed in Figure S2. Calculations performed with the single-reference methods (ADC(2), TD-B3LYP and CAM-B3LYP) locate the first three excited states (one bright and two dark states) of pyr-graphitic-1 in the range of 1.3 to 2.6 eV quite well in comparison to the MR methods DFT/MRCI and SC-NEVPT2. However, the next excited state is separated by an energy gap of ~ 2 eV in all these three cases, in stark contrast to the results obtained by the MR methods, where five and six, respectively, doubly-excited states appear, following the lowest three states. The lowest doubly-excited state was found to be a $HOMO^2 \rightarrow LUMO^2$ excitation. This gap shown by the SR methods is explained by the inability of describing states with higher than single excitations. A similar picture is observed also for pyr-graphitic-3. In this case the ground state has more radical character. Therefore, the three lowest singly excited energies are located at even lower energies. For example, the excitation energy to S_1 is quite small (0.43 eV with DFT/MRCI) as compared to 1.40 eV for pyr-graphitic-1, which has a KEK ground state structure.

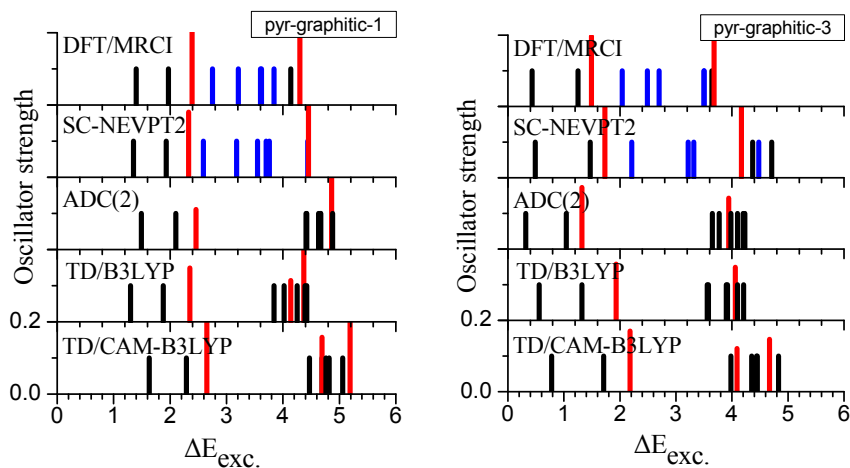


Figure 7 Excitation spectra of pyr-graphitic-1 and pyr-graphitic-3, calculated at the DFT/MRCI, SC-NEVPT2, ADC(2), TD-B3LYP and CAM-TD-B3LYP levels. Bright singly excited states are highlighted in red, dark doubly excited states are in blue and the remaining dark singly excited states are in black. Dark states are defined as having $f < 0.1$. Note that the dark states have not been drawn according to their actual f value but with the threshold value of $f = 0.1$ in order to assure their visibility in the graphics.

Figure 8 gives a global overview of the evolution of the shifts of the lowest five excited singlet states for the doped graphitic structures in comparison to pyrene. The smallest excitation energy for the bright state (red line) is found for pyr-graphitic-3 with 1.5 eV, which amounts to a shift of 2.3 eV in comparison to the bright L_a state in pyrene.

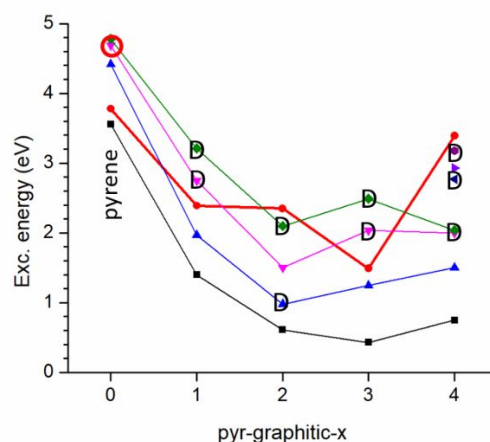


Figure 8. Evolution of different types of excited states in dependence of the different cases of graphitic doping by means of the DFT/MRCI approach: red line and red open circle – bright states ($f > 0.1$); other lines - dark states; D indicates significant contribution of doubly-excited configurations.

3.2.2 Graphitic-edge structures

Figure 9 shows an overview of the S_1 excitation energies calculated with the different computational methods used in this work. The complete list of excitation energies computed for the first ten states, oscillator strengths and the classification in terms of single (S) and double (D) excitations can be found in Table S2. The graphs displayed in Figure 9 show good consistency between the different methods. The peaks in the figure indicate large excitation energies close to or even higher than the value for the L_b state of pyrene. It is interesting to note that the corresponding isomers (pyr-graphitic-edge-3, -5, -7, -10, -11 and -14) constitute exactly group I of the most stable structures. The group I pyr-graphitic-edge-3 structure is also found to be included in this list even though it does not belong to the most stable ground state structures. The group III structures pyr-graphitic-edge-6, -8 and -13, characterized as Clar(DR), are those with the smallest S_1 excitation energies below or close to one eV. However, it should be mentioned that also pyr-graphitic-edge-4 (group II, KEK, Clar(DR)) shows a small excitation energy close to one eV due to its biradical character.

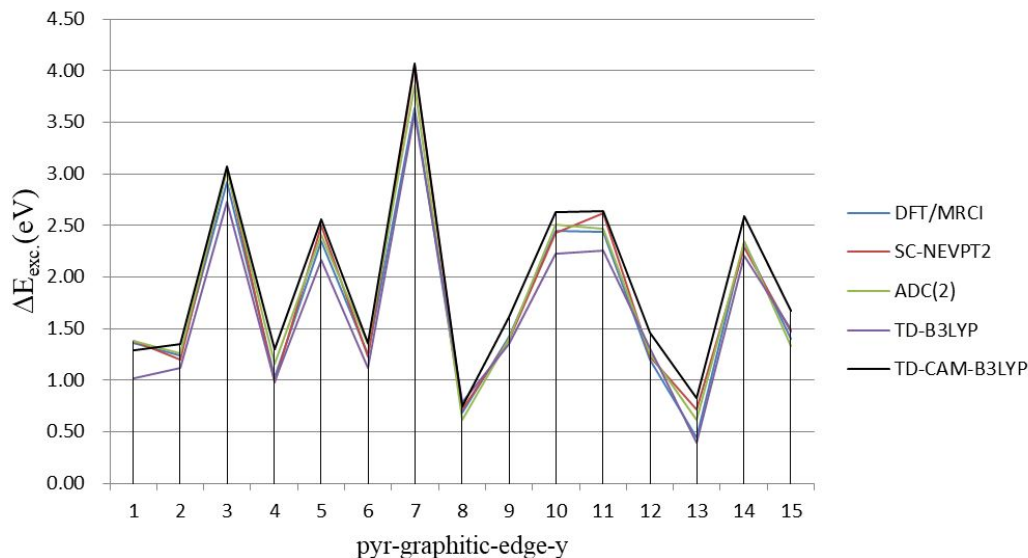


Figure 9 Vertical excitation energies to the S_1 state for graphitic-edge doping structures for all methods using the def2-TZVP basis (pyrene exp. (L_b) 3.41 eV⁸⁷).

Figure 10 shows a characteristic example of the overall spectrum for each graphitic-edge doping group. The spectra of the remaining graphitic-edge doping cases are displayed in Figure S3. For the group-I case pyr-graphitic-edge-5, quite good agreement between different methods is found. The states S_5 and S_6 of the DFT/MRCI calculation are Rydberg states and are not of interest in the present context. Doubly-excited states appear only higher in the spectrum. With a few exceptions, the lowest doubly excited state was found to have $HOMO^2 \rightarrow LUMO^2$ character. Moving on the examples for the other two groups, one notes that the bright state does not significantly change its position, instead several dark states are stabilized at lower energies. The bright doubly-excited state shown for the pyr-graphitic-edge-1 structure exhibits actually a strong mixture with singly-excited configurations explaining the strong intensity. In Figure 11 a graphical overview of the spectra of all pyr-graphitic-edge cases is given based on DFT/MRCI calculations. It shows the systematic shift of dark states to lower energies and the occurrence of several doubly excited states in the low-energy region.

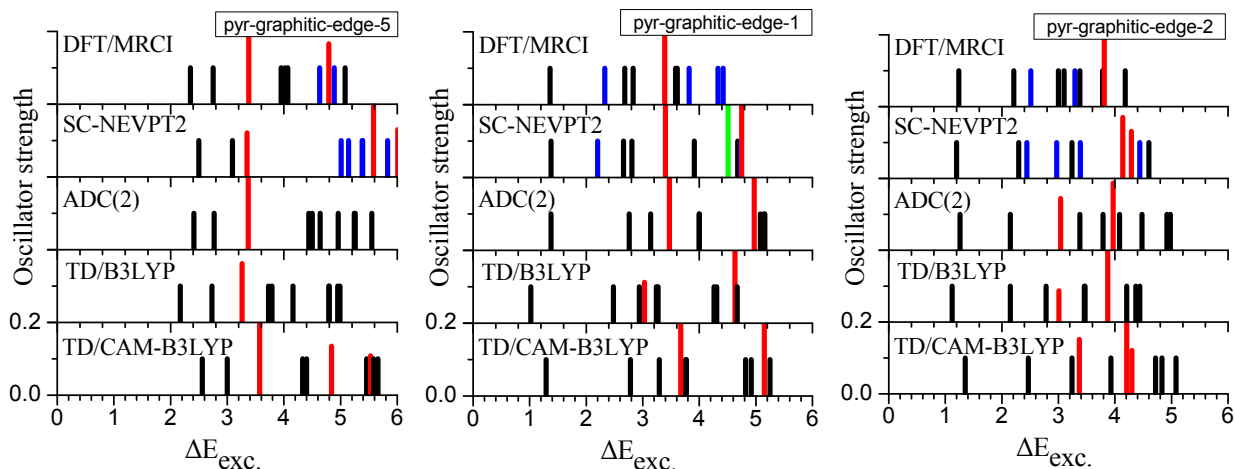


Figure 10 Excitation spectrum of a) pyr-graphitic-edge-5 (group I), b) pyr-graphitic-edge-1 (group II), and c) pyr-graphitic-edge-2 (group III), calculated at the DFT/MRCI, SC-NEVPT2, ADC(2), TD-B3LYP and CAM-TD-B3LYP levels. Bright singly excited states are highlighted in red, a bright doubly excited state is highlighted in green, dark doubly excited states are in blue and the remaining dark singly excited states are in black. Dark states are defined as having $f < 0.1$. Note that the dark states have not been drawn according to their actual f value but with the threshold value of $f = 0.1$ in order to assure their visibility in the graphics.

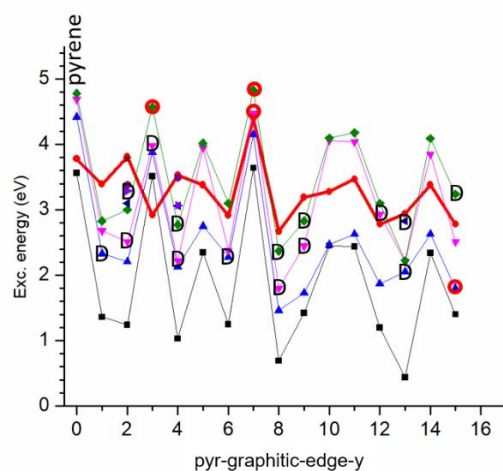


Figure 11 Evolution of different types of excited states in dependence of the different cases of graphitic-edge doping by means of the DFT/MRCI approach: red line and red open circles – bright states ($f > 0.1$); other lines - dark states; D indicates significant contribution of doubly-excited configurations.

3.2.3 Pyridinic structures

One difference to the two doping cases discussed above is the occurrence of lone pairs and corresponding $n \rightarrow \pi^*$ transitions. Figure 12 shows the evolution of the S_1 excitation energies with the different structures computed with different methods. The complete list of excitation energies computed for the first ten states, oscillator strengths and the classification in terms of single (S) and double (D) excitations can be found in Table S4. As has already been noted in the discussion of the ground-state stabilities, a more uniform behavior in the S_1 excitation energies and similarity to pyrene is observed due to the fact that the nitrogen contributes only one electron to the π system and thus the number of π electrons is not changed as compared to pyrene. The general trend in the S_1 excitation energies across all doped structures is very well reproduced by all methods. ADC(2) and TD-B3LYP come closest to the DFT/MRCI benchmark results. SC-NEVPT2 deviates most toward smaller excitation energies and CAM-B3LYP toward larger energies. Outstanding doping structures in terms of decreased energy gaps are the pyr-pyridinic-3 and -7 structures which have adjacent N atoms. Figure 13 provides an overview of the overall spectrum for two doping cases in order to show the similarity to the pyrene spectrum. The spectra of the remaining pyridinic doping cases are displayed in Figure S4. Except for one transition in pyr-pyridinic-7, the spectrum starts at ~ 4 eV in contrast to the graphitic (Figure 7) and graphitic-edge (Figure 10) spectra, which extend to much lower excitation energies. From Figure 14 the evolution of excitation energies for several states can be seen. The above-mentioned decreased excitation energies for the pyr-pyridinic-3 and -7 cases is traced back to $n\text{-}\pi^*$ states. The latter states do not appear as lowest ones in the other cases, but are quite abundant in higher excited states.

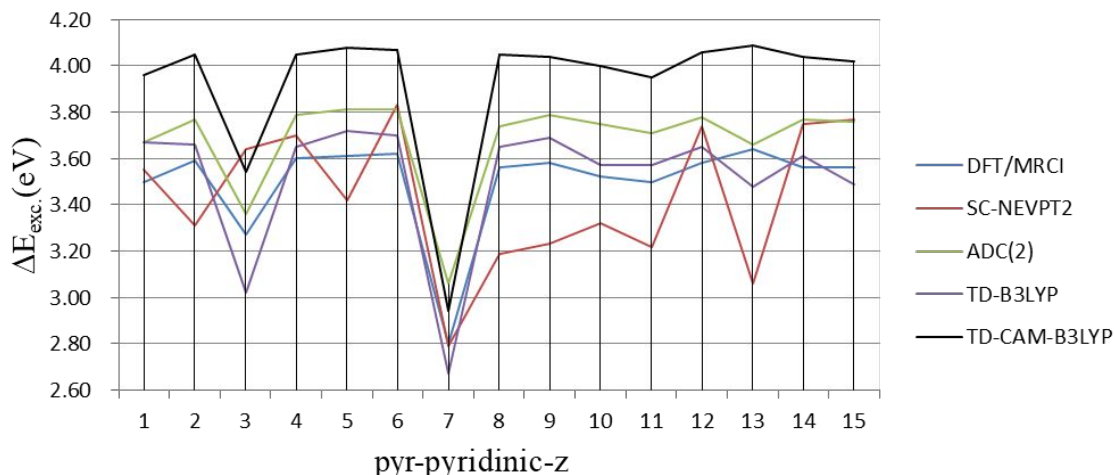


Figure 12 Vertical excitation energies to the S_1 state for pyr-pyridinic doping structures for all methods using the def2-TZVP basis (pyrene exp. (L_b) 3.41 eV⁸⁷).

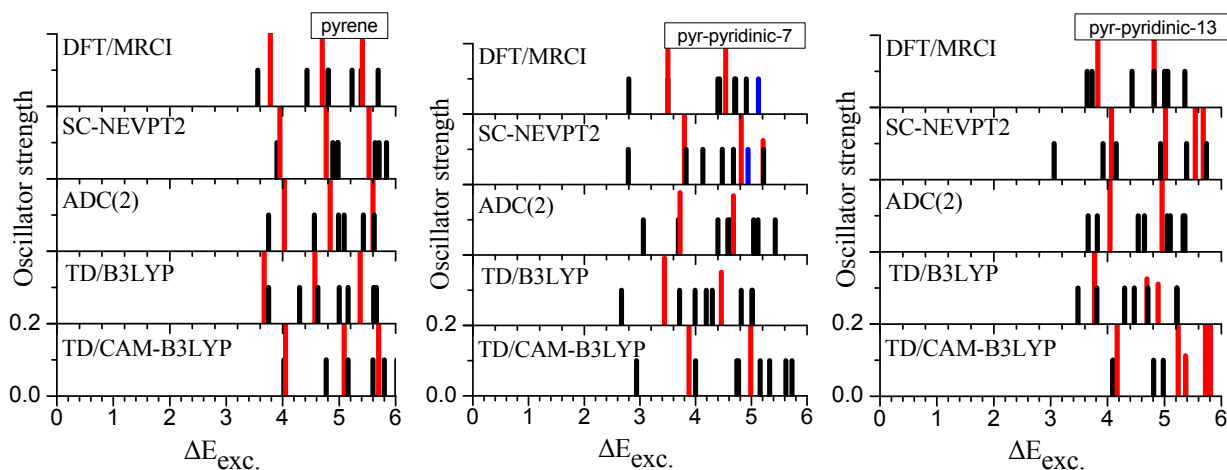


Figure 13 Excitation spectrum of a) pyrene, b) pyr-pyridinic-7, and c) pyr-pyridinic-13, calculated at the DFT/MRCI, SC-NEVPT2, ADC(2), TD-B3LYP and CAM-TD-B3LYP levels. Bright singly excited states are highlighted in red, dark doubly excited states are in blue and the remaining dark singly excited states are in black. Dark states are defined as having $f < 0.1$. Note that the dark states have not been drawn according to their actual f value but with the threshold value of $f = 0.1$ in order to assure their visibility in the graphics.

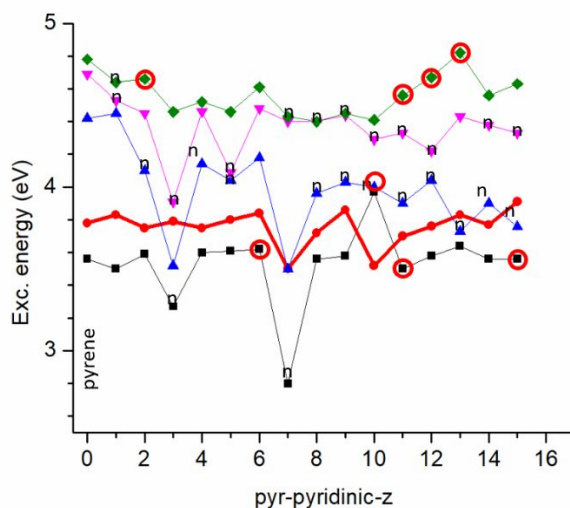


Figure 14 Evolution of different types of excited states in dependence of the different cases of pyridinic doping calculated by means of the DFT/MRCI approach: red line and red open circles – bright states ($f > 0.1$); other lines - dark states; n indicates $n-\pi^*$ states.

4 Conclusions:

Our calculations on N-doped pyrene structures show that a great variation in the relative ground-state stability and in the red shifts in the UV spectra can be achieved. From the three types of N-doping, graphitic, graphitic-edge and pyridinic, the first two are the ones with significantly larger variation. The red shifts for graphitic doping are substantial and amount to 2.2 to 3.2 eV, depending on the doping case. The lowest few states are usually dark states with oscillator strengths below 0.1. The lowest bright state following them is also strongly red-shifted by about 2 eV. The dependence of the S_1 excitation energy on the graphitic-edge doping cases shows more variation, ranging from a blue shift to significant red shifts similar to the graphitic doping. Between these two limits a number of intermediate S_1 excitation energies can be found. The energetic shifts for pyridinic doping are in general significantly smaller and resemble more the original pyrene spectrum.

This picture has been substantiated by using a series of different methods, the most advanced ones are based on multireference technologies, which provide the basis for comparison with single-

reference methods including TDDFT. It is important to observe that the few lowest states can be described well as single excitations, which simplifies the computational tasks considerably. However, it should be noted that also several double excitations occur which are clearly missing in the single-reference case. Additionally, doubly excited configurations are found to mix in several cases with singly excited configurations, so that the transitions to these states acquire non-negligible oscillator strengths. This means that especially internal conversion processes to S_1 , which will pass through several states, can be biased when using popular single-reference methods such as TDDFT or ADC(2).

The differences between the graphitic and graphitic-edge doping on one side and the pyridinic doping on the other side can be explained overall that in the first case the number of π electrons is increased by two as compared to pyrene since each N atom contributes two electrons to the π system instead of one, which the original C atoms had contributed. In the latter case the number of π electrons remains unchanged. This difference has an important influence in obtaining desired significant red shifts in the UV spectra, which are primarily found in the first case. Pyridinic doping is not well suited for that purpose. Qualitative analysis according to valence bond theory in combination with Clar's sextet rule and the distance between the two N atoms in terms of separating atoms provide simple, but useful tools to classify the doping process. Additionally, the HOMA index was used to assess the aromaticity in quantitative terms. This concept worked very well especially for finding cases of either strong diradicaloid character or dominant Kekulé structures on the other hand. Structures with strong diradical character are found when the two nitrogen atoms are located in the same sublattice where no Kekulé structure can be constructed. The presence of a Clar sextet enhances this effect. In such cases remarkably small S_1 excitation energies of around 1 to 0.5 eV or less, ranging into the infrared region, are observed. It has also been found that increasing the interatomic distance between the N atoms (NS values) enhances the stability of the doped structures in general. The NS values indicate also the relative location of the N atoms in the two sublattices of the alternant π conjugated system of pyrene. The stability of isomers with N atoms located in different sublattices (NS even) appeared to be preferred because of the possibility of constructing Kekulé structures. Overall, this qualitative analysis appeared very useful in rationalizing the relative stabilities of the different isomers and also respective shifts in the UV spectra.

Conflicts of interest

There are no conflicts to declare.

Acknowledgements

We are grateful for support from the School of Pharmaceutical Science and Technology (SPST), Tianjin University, Tianjin, China, including computer time on the SPST computer cluster Arran. This work was supported by the Center for Integrated Nanotechnologies (Project No. 2019BC0064), an Office of Science User Facility operated for the U.S. Department of Energy Office of Science by Los Alamos National Laboratory (Contract No. 89233218CNA000001) and Sandia National Laboratories (Contract No. DE-NA-0003525). D.N. acknowledges the support of the Czech Science Foundation (GA18-09914S). This work was also a part of the research project RVO (61388963) of the IOCB of the Czech Academy of Sciences. M.O. acknowledges support from the Ministry of Education, Youth and Sports of the Czech Republic (project CZ.02.1.01/0.0/0.0/16_019/0000754).

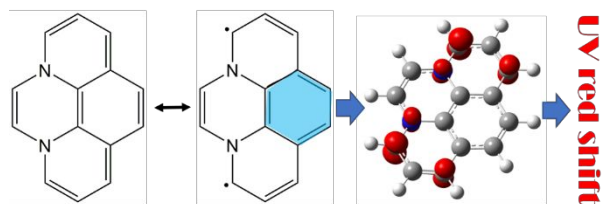
References

1. Q. Zhao, W. Song, B. Zhao and B. Yang, *Mater. Chem. Front.*, 2020, **4**, 472-488.
2. Q. Liu, J. Sun, K. Gao, N. Chen, X. Sun, D. Ti, C. Bai, R. Cui and L. Qu, *Mater. Chem. Front.*, 2020, **4**, 421-436.
3. Q. Jia, Z. Zhao, K. Liang, F. Nan, Y. Li, J. Wang, J. Ge and P. Wang, *Mater. Chem. Front.*, 2020, **4**, 449-471.
4. D. Rodriguez-Padron, R. Luque and M. J. Munoz-Batista, *Top. Curr. Chem.*, 2019, **378**, 3.
5. S. Bayda, M. Adeel, T. Tuccinardi, M. Cordani and F. Rizzolio, *Molecules*, 2019, **25**, 112.
6. M. Kaur, M. Kaur and V. K. Sharma, *Adv. Colloid Interface Sci.*, 2018, **259**, 44-64.
7. S. Chen, X. Chen, T. Xia and Q. Ma, *Biosens. Bioelectron.*, 2016, **85**, 903-908.
8. Y. Li, Y. Zhao, H. Cheng, Y. Hu, G. Shi, L. Dai and L. Qu, *J. Am. Chem. Soc.*, 2012, **134**, 15-18.
9. T. Sharifi, G. Hu, X. Jia and T. Wagberg, *ACS Nano*, 2012, **6**, 8904-8912.
10. L. Lai, J. R. Potts, D. Zhan, L. Wang, C. K. Poh, C. Tang, H. Gong, Z. Shen, J. Lin and R. S. Ruoff, *Ener. & Environ. Sci.*, 2012, **5**, 7936-7942.
11. D.-W. Wang and D. Su, *Ener. & Environ. Sci.*, 2014, **7**, 576-591.
12. K. Parvez, S. Yang, Y. Hernandez, A. Winter, A. Turchanin, X. Feng and K. Müllen, *ACS Nano*, 2012, **6**, 9541-9550.
13. V. C. Hoang, K. Dave and V. G. Gomes, *Nano Energy*, 2019, **66**.
14. T. F. Yeh, C. Y. Teng, S. J. Chen and H. Teng, *Adv. Mater.*, 2014, **26**, 3297-3303.
15. A. Cai, Q. Wang, Y. Chang and X. Wang, *J. Alloys Compd.*, 2017, **692**, 183-189.
16. M. Yan, F. Zhu, W. Gu, L. Sun, W. Shi and Y. Hua, *RSC Advances*, 2016, **6**, 61162-61174.
17. C. Hu, M. Li, J. Qiu and Y. P. Sun, *Chem. Soc. Rev.*, 2019, **48**, 2315-2337.
18. L. Ruiyi, J. Yuanyuan, Z. Xiaoyan, L. Zaijun, G. Zhiguo, W. Guangli and L. Junkang, *Electrochim. Acta*, 2015, **178**, 303-311.
19. M. Kaur, S. K. Mehta and S. K. Kansal, *Sensors and Actuators B: Chemical*, 2017, **245**, 938-945.
20. B. J. Moon, D. Jang, Y. Yi, H. Lee, S. J. Kim, Y. Oh, S. H. Lee, M. Park, S. Lee and S. Bae, *Nano Energy*, 2017, **34**, 36-46.
21. C. Xia, X. Hai, X. W. Chen and J. H. Wang, *Talanta*, 2017, **168**, 269-278.
22. M. Kaur, S. K. Mehta and S. K. Kansal, *Spectrochim. Acta A*, 2017, **180**, 37-43.
23. J. Zhou, H. Zhou, J. Tang, S. Deng, F. Yan, W. Li and M. Qu, *Microchim. Acta*, 2016, **184**, 343-368.
24. W. Cai, T. Zhang, M. Xu, M. Zhang, Y. Guo, L. Zhang, J. Street, W.-J. Ong and Q. Xu, *J. Mater. Chem. C*, 2019, **7**, 2212-2218.

25. K. Hola, Y. Zhang, Y. Wang, E. P. Giannelis, R. Zboril and A. L. Rogach, *Nano Today*, 2014, **9**, 590-603.
26. Z. Zhu, Y. Zhai, Z. Li, P. Zhu, S. Mao, C. Zhu, D. Du, L. A. Belfiore, J. Tang and Y. Lin, *Materials Today*, 2019, **30**, 52-79.
27. W. Gao, Y. Ma, Y. Zhou, H. Song, L. Li, S. Liu, X. Liu, B. Gao, C. Liu and K. Zhang, *Mater. Lett.*, 2018, **216**, 84-87.
28. M. Yang, B. Li, K. Zhong and Y. Lu, *J. Mater. Sci.*, 2017, **53**, 2424-2433.
29. S. R. M. Santiago, Y. A. Wong, T. N. Lin, C. H. Chang, C. T. Yuan and J. L. Shen, *Opt. Lett.*, 2017, **42**, 3642-3645.
30. Y. Xiong, J. Schneider, C. J. Reckmeier, H. Huang, P. Kasak and A. L. Rogach, *Nanoscale*, 2017, **9**, 11730-11738.
31. B. C. M. Martindale, G. A. M. Hutton, C. A. Caputo, S. Prantl, R. Godin, J. R. Durrant and E. Reisner, *Angew Chem Int Ed Engl*, 2017, **56**, 6459-6463.
32. C.-T. Hsieh, D.-Y. Tzou, K.-Y. Hsieh and K.-M. Yin, *RSC Advances*, 2017, **7**, 18340-18346.
33. A. Sharma, T. Gadly, A. Gupta, A. Ballal, S. K. Ghosh and M. Kumbhakar, *J. Phys. Chem. Lett.*, 2016, **7**, 3695-3702.
34. S. Kim, S. W. Hwang, M.-K. Kim, D. Y. Shin, D. H. Shin, C. O. Kim, S. B. Yang, J. H. Park, E. Hwang and S.-H. Choi, *ACS Nano*, 2012, **6**, 8203-8208.
35. Y. Liang, Y. F. Shen, C. L. Liu and X. Y. Ren, *J. Lumin.*, 2018, **197**, 285-290.
36. X. Zhai, P. Zhang, C. Liu, T. Bai, W. Li, L. Dai and W. Liu, *Chem. Commun.*, 2012, **48**, 7955.
37. J. Wang, P. Zhang, C. Huang, G. Liu, K. C. Leung and Y. X. Wang, *Langmuir*, 2015, **31**, 8063-8073.
38. M. Fu, F. Ehrat, Y. Wang, K. Z. Milowska, C. Reckmeier, A. L. Rogach, J. K. Stolarczyk, A. S. Urban and J. Feldmann, *Nano Lett.*, 2015, **15**, 6030-6035.
39. Y.-Q. Zhang, D.-K. Ma, Y. Zhuang, X. Zhang, W. Chen, L.-L. Hong, Q.-X. Yan, K. Yu and S.-M. Huang, *J. Mater. Chem.*, 2012, **22**.
40. X. Chen, Q. Jin, L. Wu, C. Tung and X. Tang, *Angew. Chem. Int. Edit.*, 2014, **53**, 12542-12547.
41. Z. Qian, J. Ma, X. Shan, H. Feng, L. Shao and J. Chen, *Chem. Eur. J.*, 2014, **20**, 2983-2983.
42. Z. Qian, J. Ma, X. Shan, H. Feng, L. Shao and J. Chen, *Chemistry*, 2014, **20**, 2254-2263.
43. S. Sarkar, M. Sudolská, M. Dubecký, C. J. Reckmeier, A. L. Rogach, R. Zbořil and M. Otyepka, *J. Phys. Chem. C* 2016, **120**, 1303-1308.
44. K. Hola, M. Sudolska, S. Kalytchuk, D. Nachtigallova, A. L. Rogach, M. Otyepka and R. Zboril, *ACS Nano*, 2017, **11**, 12402-12410.
45. X. Niu, Y. Li, H. Shu and J. Wang, *Nanoscale*, 2016, **8**, 19376-19382.

46. S. S. R. Merden, W. Y. Ann, L. Tzu-Neng, C. Chiao-Hsin, Y. Chi-Tsu and S. Ji-Lin, *Opt. Lett.*, 2017, **42**, 3642-3645.
47. M. Sudolská, M. Dubecký, S. Sarkar, C. J. Reckmeier, R. Zbořil, A. L. Rogach and M. Otyepka, *J. Phys. Chem. C* 2015, **119**, 13369-13373.
48. M. Sudolská and M. Otyepka, *Appl. Mater. Today*, 2017, **7**, 190-200.
49. C. K. Lin, *J. Comput. Chem.*, 2018, **39**, 1387-1397.
50. A. Das, T. Müller, F. Plasser, D. B. Krisiloff, E. A. Carter and H. Lischka, *J. Chem. Theory Comput.*, 2017, **13**, 2612-2622.
51. R. Nieman, N. J. Silva, A. J. A. Aquino, M. M. Haley and H. Lischka, *J. Org. Chem.*, 2020, **85**, 3664-3675.
52. M. Pinheiro, L. F. A. Ferrao, F. Bettanin, A. J. A. Aquino, F. B. C. Machado and H. Lischka, *Phys. Chem. Chem. Phys.*, 2017, **19**, 19225-19233.
53. A. Das, M. Pinheiro, Jr., F. B. C. Machado, A. J. A. Aquino and H. Lischka, *ChemPhysChem*, 2018, **19**, 2492-2499.
54. S. Grimme and M. Waletzke, *J. Chem. Phys.*, 1999, **111**, 5645-5655.
55. I. Lyskov, M. Kleinschmidt and C. M. Marian, *J. Chem. Phys.*, 2016, **144**, 034104.
56. C. M. Marian, A. Heil and M. Kleinschmidt, *Wires Comput. Mol. Sci.*, 2019, **9**, e1394.
57. A. Heil, M. Kleinschmidt and C. M. Marian, *J. Chem. Phys.*, 2018, **149**, 164106.
58. C. Angeli, R. Cimiraglia and J.-P. Malrieu, *Chem. Phys. Lett.*, 2001, **350**, 297-305.
59. C. Angeli, R. Cimiraglia and J.-P. Malrieu, *J. Chem. Phys.*, 2002, **117**, 9138-9153.
60. J. Schirmer, *Phys. Rev. A*, 1982, **26**, 2395-2416.
61. A. B. Trofimov and J. Schirmer, *J. Phys. B: At., Mol. Opt. Phys.*, 1995, **28**, 2299-2324.
62. A. D. P. Becke, *Phys. Rev. A*, 1988, **38**, 3098-3100.
63. T. Yanai, D. P. Tew and N. C. Handy, *Chem. Phys. Lett.*, 2004, **393**, 51-57.
64. F. Bettanin, L. F. A. Ferrao, M. Pinheiro, Jr., A. J. A. Aquino, H. Lischka, F. B. C. Machado and D. Nachtigallova, *J. Chem. Theory Comput.*, 2017, **13**, 4297-4306.
65. B. Shi, D. Nachtigallova, A. J. A. Aquino, F. B. C. Machado and H. Lischka, *J. Chem. Phys.*, 2019, **150**, 124302.
66. B. Shi, D. Nachtigallova, A. J. A. Aquino, F. B. C. Machado and H. Lischka, *Phys. Chem. Chem. Phys.*, 2019, **21**, 9077-9088.
67. B. Shi, D. Nachtigallova, A. J. A. Aquino, F. B. C. Machado and H. Lischka, *J. Phys. Chem. Lett.*, 2019, **10**, 5592-5597.
68. M. Pinheiro Jr, F. B. C. Machado, F. Plasser, A. J. A. Aquino and H. Lischka, *J. Mater. Chem. C*, 2020, **8**, 7793-7804.
69. E. Clar, *The Aromatic Sextet*, Wiley, London, 1972.
70. S. Grimme, J. Antony, S. Ehrlich and H. Krieg, *J. Chem. Phys.*, **132**, 154104-154100.

71. C. Møller and M. S. Plesset, *Phys. Rev.*, 1934, **46**, 618-622.
72. Y. Jung, R. C. Lochan, A. D. Dutoi and M. Head-Gordon, *J. Chem. Phys.*, 2004, **121**, 9793-9802.
73. C. Riplinger, P. Pinski, U. Becker, E. F. Valeev and F. Neese, *J. Chem. Phys.*, 2016, **144**, 024109.
74. G. D. P. III and R. J. Bartlett, *J. Chem. Phys.*, 1982, **76**, 1910-1918.
75. K. Raghavachari, G. W. Trucks, J. A. Pople and M. Head-Gordon, *Chem. Phys. Lett.*, 1989, **157**, 479-483.
76. F. Weigend and R. Ahlrichs, *Phys. Chem. Chem. Phys.*, 2005, **7**, 3297-3305.
77. C. Hättig and F. Weigend, *J. Chem. Phys.*, 2000, **113**, 5154-5161.
78. A. D. Becke, *J. Chem. Phys.*, 1993, **98**, 1372-1377.
79. J. Kruszewski and T. M. Krygowski, *Tetrahedron Lett.*, 1972, **13**, 3839-3842.
80. T. M. Krygowski, *J. Chem. Inf. Comput. Sci.*, 1993, **33**, 70-78.
81. K. Takatsuka, T. Fueno and K. Yamaguchi, *Theor. Chim. Acta*, 1978, **48**, 175-183.
82. V. N. Staroverov and E. R. Davidson, *Chem. Phys. Lett.*, 2000, **330**, 161-168.
83. R. Ahlrichs, M. Bär, M. Häser, H. Horn and C. Kölmel, *Chem. Phys. Lett.*, 1989, **162**, 165-169.
84. M. J. Frisch, G. W. Trucks, H. B. Schlegel, G. E. Scuseria, M. A. Robb, J. R. Cheeseman, G. Scalmani, V. Barone, B. Mennucci, G. A. Petersson, H. Nakatsuji, M. Caricato, X. Li, H. P. Hratchian, A. F. Izmaylov, J. Bloino, G. Zheng, J. L. Sonnenberg, M. Hada, M. Ehara, K. Toyota, R. Fukuda, J. Hasegawa, M. Ishida, T. Nakajima, Y. Honda, O. Kitao, H. Nakai, T. Vreven, J. A. Montgomery Jr., J. E. Peralta, F. Ogliaro, M. J. Bearpark, J. Heyd, E. N. Brothers, K. N. Kudin, V. N. Staroverov, R. Kobayashi, J. Normand, K. Raghavachari, A. P. Rendell, J. C. Burant, S. S. Iyengar, J. Tomasi, M. Cossi, N. Rega, N. J. Millam, M. Klene, J. E. Knox, J. B. Cross, V. Bakken, C. Adamo, J. Jaramillo, R. Gomperts, R. E. Stratmann, O. Yazyev, A. J. Austin, R. Cammi, C. Pomelli, J. W. Ochterski, R. L. Martin, K. Morokuma, V. G. Zakrzewski, G. A. Voth, P. Salvador, J. J. Dannenberg, S. Dapprich, A. D. Daniels, Ö. Farkas, J. B. Foresman, J. V. Ortiz, J. Cioslowski and D. J. Fox, Gaussian, Inc., Wallingford, CT, USA2009.
85. F. Neese, *Wires Comput. Mol. Sci.*, 2018, **8**, e1327.
86. C. A. Coulson and G. S. Rushbrooke, *Proc. Camb. Phil. Soc.*, 1940, **36**, 193-200.
87. R. S. Becker, I. S. Singh and E. A. Jackson, *J. Chem. Phys.*, 1963, **38**, 2144-2171.
88. S. Shirai and S. Inagaki, *RSC Advances*, 2020, **10**, 12988-12998.

Table of Contents Entry

Nitrogen doping leads to biradicaloid character and subsequent UV red shift